Investigation of thermal properties of blast furnace slag to improve process energy efficiency

Sara Yasipourtehrani, Vladimir Strezov[*], Sergey Bliznyukov, Tim Evans

Department of Environmental Sciences, Faculty of Science and Engineering, Macquarie University, NSW 2109, Australia

ABSTRACT

Blast furnace slag (BFS) is the main by-product of iron making and is produced in large amounts worldwide. To improve energy use, it is necessary to understand the thermal behaviour of slags under differing compositions at varying temperatures. This study determines the thermal properties and behaviour of selected slag samples using several experimental techniques, including high temperature Hot Stage Scanning Electron Microscopy (HS-SEM), and Computer Aided Thermal Analysis (CATA). Further methods, such as Energy Dispersive Spectroscopy (EDS) and Fourier Transfer Infrared Spectroscopy (FTIR) were applied to determine the chemical content and nature of the studied BFS samples. Comparing the chemical composition of the slags and their thermal behaviour, the effect of magnesium oxide and aluminium oxide was evident on the crystallisation and fluidity of the molten slag. Additionally, the content of silicon dioxide had an effect on the crystallisation temperature and network strength.

© 2017 Elsevier Ltd. All rights reserved.

1. Introduction

Iron is one of the most common metals used worldwide. The main raw materials required for production of iron are iron ore, coal, limestone and recycled steel. The amount of iron slag produced in 2012 was 270—320 Mt and this amount increases every year as the demand increases (Sadek, 2014). China is the largest producer of iron ore at 1.5 Gt per annum and Australia is the second largest with 660 Mt of iron ore produced per year (Iron Ore and Global market, 2015). Any improvement in the efficiency of energy recovery and recycling in the iron making process, including the recycling of the by-product slag, will have positive global implications, both economically and environmentally (Zhao et al., 2015).

The iron and steel making process generates significant amounts of waste materials, such as slags (Kan et al., 2015). Because of landfill restrictions and other environmental considerations, possible recycling of these materials or development of new by-products have become principal incentives for this industry (Francis, 2005), aiming to preserve the natural resources and, where possible, conserve energy where material properties and characteristics are suitable (Motz and Geiseler, 2001).

One of the steps in the iron making process is to heat the pig iron up to 1500 °C for the next phase of steel-making. In this process a significant amount of energy is transferred to the blast furnace slag (BFS), which reaches temperatures of around 1500 °C at the end of this process (Sadek, 2014). Utilising the waste heat energy from the slag to contribute to heating the pig iron would achieve better energy efficiency and sustainability of the blast furnace steel-making process. To improve energy use, it is necessary to understand behaviour of the slags with different compositions and at varying temperatures.

The properties of different blast furnace slags (BFS) vary and are determined by the ore type, ash of the coke and the process operating conditions. Slag can be considered as a resource not used before and, depending on its properties, its use is possible in another part of the industry (Dimitrova, 1995), which helps to reduce environmental contamination, energy use and production costs (Ozturk and Gultekin, 2015). The possible reuses of BFS depend on the slag properties and heat treatment of the molten slag. Accordingly, it is necessary to enhance the knowledge of the phase chemistry of slag to optimise the productivity and performance in recycling (Jak and Hayes, 2004).

In the blast furnace (BF) gangue and non-metallic impurities are separated from the iron ore with the final products being pig iron and slag (Dippenaar, 2005). Pig iron and molten slag accumulate at the hearth of the BF, and the slag is positioned above the pig iron, as its density is lower than iron (Ito et al., 2014). There are some difficulties associated with draining the slag from the BF as it has high viscosity while in the lower temperature zones of the furnace this viscosity increases (Ito et al., 2014).

When slag is tapped from the furnace it has high temperature and different methods of cooling will affect the slag composition (Dippenaar, 2005). Appropriate treatment of high-temperature slag with a suitable cooling process improves the slag properties and its applications for recycling (Liapis and Papayianni, 2015).

The molten slag has two separate final solid states; (i) crystalline phase, which comes from the slow cooling of the molten slag, and (ii) glassy, amorphous or vitreous phase, which is caused by quenching or rapid cooling of the slag (Kriskova et al., 2013). Table 1 demonstrates the most important type of slag as a by-product and the end use of these materials.

There have been many attempts to recover the energy from slag for use as heat, electricity generation or fuel, but none of them has been commercialised yet (Baati et al., 2011). The reason for this is that the industry is more focused on quenching the slag and promoting the formation of glassy phases for use in cement rather than recovering the energy. If energy recovery is the goal of slag quenching, then the slag will not be cooled fast enough to manufacture the preferred glassy and amorphous phase. The water quenching technique produces glassy BFS (Crossin, 2015). The air-cooling technique is applied for some lower value applications, such as the production of bitumen (Crossin, 2015).

During slag cooling, the solid phases appear and increase the viscosity (Kim et al., 2004). The composition of phases will change continually when the temperature is reduced from liquid to solid. The melting point is one of the critical properties of BFS related to the chemical content. The BFS melting point and liquid temperature increase by increasing the basicity ratio (Dai and Zhang, 2012), which is the ratio of CaO to SiO_2. The basicity is an important slag characteristic as this ratio affects crystallisation (Kuo et al., 2007).

High amounts of SiO_2 reduce the melting point and retard the formation of crystals in the slag, increasing the strength and water permeability. For this reason, engineering the slag cooling process so that energy is recovered, while producing the favourable slag properties for its further use or recycling, is an essential part in designing cleaner iron and steelmaking production.

The aim of this research is to determine how changes of chemical content during slag melting and solidification processes of different industrial BFS affect the underlying thermal properties and energy use. In this research, the thermal properties of BFS were determined and slag melting and solidification phenomena observed, such as crystal formation and glassy phase segregation. The changes of chemical content during melting and cooling process of different industrial BFS were additionally determined. The understanding and insights of the high temperature behaviour and properties of blast furnace slag assist improvement of the BF performance and optimisation of heat energy recovery of slags without detriment to the higher value use as an ingredient in the manufacture of cement or other applications.

Table 2
Chemical composition of the samples.

Slag	TFe	SiO_2	CaO	MgO	Al_2O_3	MnO	TiO_2	Basicity
Sample A	0.43	35.93	40.41	8.38	13.54	0.26	0.5	1.12
Sample B	0.35	33.31	40.94	8.46	14.99	0.26	0.57	1.22
Sample R	0.39	30.78	33.83	13.34	19.01	0.84	0.97	1.09

2. Materials and methods

2.1. Materials

The samples used in this study were BFS supplied from iron-making BF plants in China. For minimizing variability, each sample was ground into a fine powder and mixed to form homogeneous sub-sample. A standard ring mill batch pulverizer was used to grind the samples to fine powder. The particle size distribution for each sample after grinding was between 10 and 100 μm determined with SEM imaging. The standard chemical analysis of the samples determined with X-ray fluorescence spectroscopy is presented in Table 2.

2.2. Analytical methods

In this research a variety of instruments were used for studying the thermal properties of the BFS, which include Hot Stage Scanning Electron Microscope (HS-SEM), Energy Dispersive Spectroscopy (EDS), Computer Aided Thermal Analysis (CATA), and Fourier Transform Infrared (FTIR) Spectroscopy.

2.2.1. High temperature hot stage scanning electron microscopy (HS-SEM)

The SEM used in this study was a JEOL JXA-840 Scanning Microanalyzer, while stage modifications, high temperature furnace and appropriate detector system were custom built before the commencement of this work.

In this instrument, each sample was heated up to 1500 °C inside the microscope chamber, and the heating process was recorded to monitor the morphological changes of the sample during heating with magnifications from x 12 for panoramic viewing to x 10,000 for slow scanning high resolution images and up to x 5000 for TV filming. A molybdenum strip with dimple was used as sample holder for this study, as molybdenum is a comparatively stable material against molten slag erosion.

Working distance, which is the distance between the sample and the final lens and typically set to 12 mm, was increased to 25 mm in this study, because of the physical dimensions of the furnace used inside the microscope. The pressure inside the chamber was high vacuum. The appropriate voltage for the tungsten filament (heater) was rated nominally to 12 V for 100 W. The sample was then cooled down, and the formation of crystals that appeared on the molten surface during cooling was also recorded. The scintillator was modified for protection by covering with a

Table 1
Potential slag by-products and uses.

Slag By-Products	Slag Uses
Crystalline Phase (Slow Cooling)	Road base, ready-mix concrete, clinker manufacture, asphaltic concrete aggregate, fill, railroad ballast, hot mix asphalt, concrete pavement, concrete base, prevent erosion in the slope,
Amorphous Phase (Rapid Cooling)	Concrete, cementitious additive, can be mixed with Portland cement clinker to make a blended Type 1S cement, high fire-rated concrete base, lightweight fill applications over edgy soils,

metal, so the visual and infrared lights are reflected, and the electrons attracted.

A LabView data logging system (National Instruments™) was used for controlling, recording temperatures and electrical parameters as well as observing the heating process. The sample temperature inside the furnace was controlled by the change of current in a constant current power source mode. The temperature of the hot stage was monitored with two R-type thermocouples and manually controlled through a Zero Up (ZUP) 20-10 power supply manufactured by TDK Lambda. The sample was placed in the SEM and gradually heated until it melted and then cooled down with the heating and cooling sequence being visually recorded. A small cutting of gold wire was spark welded next to the sample to calibrate the thermocouple reading, as gold has well reproduced melting point temperature.

2.2.2. Energy dispersive spectroscopy (EDS)

Energy Dispersive Spectroscopy (EDS) is a technique widely used in scanning electron microscopy practice for analysing the chemical elements content in the sample and is used as an attachment to the SEM (Wagner, 1999, pp. 205). In this work EDS analysis was used to study the samples' composition before and after the slag melting process. This technique is limited to detecting the concentration of elements which are in the order of 0.1% of sample volume. EDS also assists recognition and identification of the chemical composition of the crystalline and other phases that appeared first in the solidification process. The EDS used in this study was on a JEOL6480LA SEM. In this experiment, the pressure used inside the microscope chamber was 30 Pa to avoid electrical charges on the dielectric slag samples. The accelerating voltage was 15 kV and the energy dispersion range was between 0 and 20 keV at the working distance of 10 ± 2 mm.

2.2.3. Trace element analysis

The trace element analysis was performed by the National Measurement Institute in Sydney. The analysis was performed on powdered samples using an inductively coupled plasma mass spectrometry (ICP-MS) and an inductively coupled plasma atomic emission spectrometry (ICP-AES) on BFS samples digested with HNO_3-HCl at 95–100 °C for 2 h. One control and one blank sample were used in the analysis.

2.2.4. Computer aided thermal analysis (CATA)

The CATA analysis technique was used for calculating the specific heat of the samples. The powdered sample was loaded in a silica glass tube to the packing density of 1435 kg/m^3 and surrounded by a graphite cylinder. The graphite heating element supplied the heat at the heating rate of 10 °C/min. The sample was kept under inert gas of argon, at 5 mL/min, and the sample was heated to the maximum temperature when the graphite reached 1200 °C. In this technique, three thermocouples were used for monitoring the temperature of the graphite as a control, surface of the sample and centre of the sample. The specific heat was calculated by the inverse numerical technique using the measured temperatures (Strezov, 2006). When the specific heat shows an increase in value, it means that the sample has an endothermic heat effect. However, in the exothermic reaction, the specific heat decreases.

2.2.5. Fourier transform infrared (FTIR) spectroscopy

FTIR spectroscopy is a technique that provides a fingerprint for identifying specific spectra by comparing the spectrum of a new unknown sample with the spectrum of a known sample identified and analysed before (Coates, 2000). FTIR assists in distinguishing the types of samples with differing structures, composition and changes in structure resulting from chemical modification (Madejova, 2003). The unit of measurement is wavenumber (cm^{-1}) and the wavenumber recorded is between 4000 cm^{-1} and 400 cm^{-1} (Coates, 2000). In this study, FTIR was used to investigate the changes of sample spectra when the sample was heated up to different temperatures of 25, 600, 820, 1010 and 1200 °C. The sample was initially heated to the temperatures specified by CATA results at a heating rate of 10 °C/min and under the inert gas argon at 5 mL/min. The sample was cooled down to room temperature under argon gas with the cooling rate of approximately 20 °C/min and then subjected to FTIR analysis at a Nicolet 6700 FTIR spectrometer through total 32 scans with a resolution of 4 cm^{-1}.

3. Results and discussions

3.1. Hot stage scanning electron microscopy

Each of the three samples was subjected twice to melting inside the SEM in order to investigate the melting interval and the crystals that appeared initially during the re-solidification process. The heating rate was 70 °C/min and the cooling rate was approximately 20 °C/min under vacuum conditions of the microscope. Fig. 1 shows example temperatures and SEM images recorded during heating of sample B. According to the thermocouple temperature and time data, the temperature/time differentiation was calculated, as presented in Fig. 1(a) and the melting started at 1357 °C and sample melted completely at 1439 °C. Fig. 1 (b) shows the sequence of frames from film images confirming the behaviour in the molten region. The melting behaviour started at 1357 °C. At 1441 °C temperature decreased sharply to 1400 °C and increased again due to the melting behaviour. At 1440 °C the sample was completely molten. The temperature/time differentiation and images of the melting process were compared to investigate the temperature of the initial liquid appearance (defined as solidus temperature for equilibrium conditions) of each sample, as well as the temperature of the completely melted sample (liquidus temperature in equilibrium systems).

The temperatures of initial liquid appearance for each sample are shown in Table 3. The highest starting melting temperature was for sample B, which initially melted at 1440 °C, and the lowest melting temperature was allotted to sample R, which started to melt at 1409 °C. The initial melting temperature of each sample is likely dependent on the slag chemistry and its structure.

The basicity (CaO/SiO_2) of each sample, presented in Table 3, appears to be correlated with greater initial melting temperature of the sample. Sample R, with the lowest basicity (according to the chemical composition), had lower initial temperature of melting in comparison with the other two samples. Sample B, with the highest basicity, had the highest starting melting temperature.

3.2. Energy dispersive spectroscopy

According to the EDS analysis shown in Figs. 2–4 the amount of MgO after melting and solidification reduced sharply. This indicates that the first growing crystals reject the MgO when re-ordering their structure. On the other hand, the amount of SiO_2 increased after melting and crystallisation, indicating that the first nucleated crystals absorb the SiO_2 from their surrounding melt to build their shape. In addition, only in Sample B, the amount of Al_2O_3 was reduced after the melting and crystallisation.

Each sample after the melting and cooling exhibited similar crystalline phases, as observed by the SEM and established by the EDS. In this step, similar crystallisation phases of each sample were discovered. The chemical composition of the top of the crystals and immediately around the crystals was measured, and the chemical
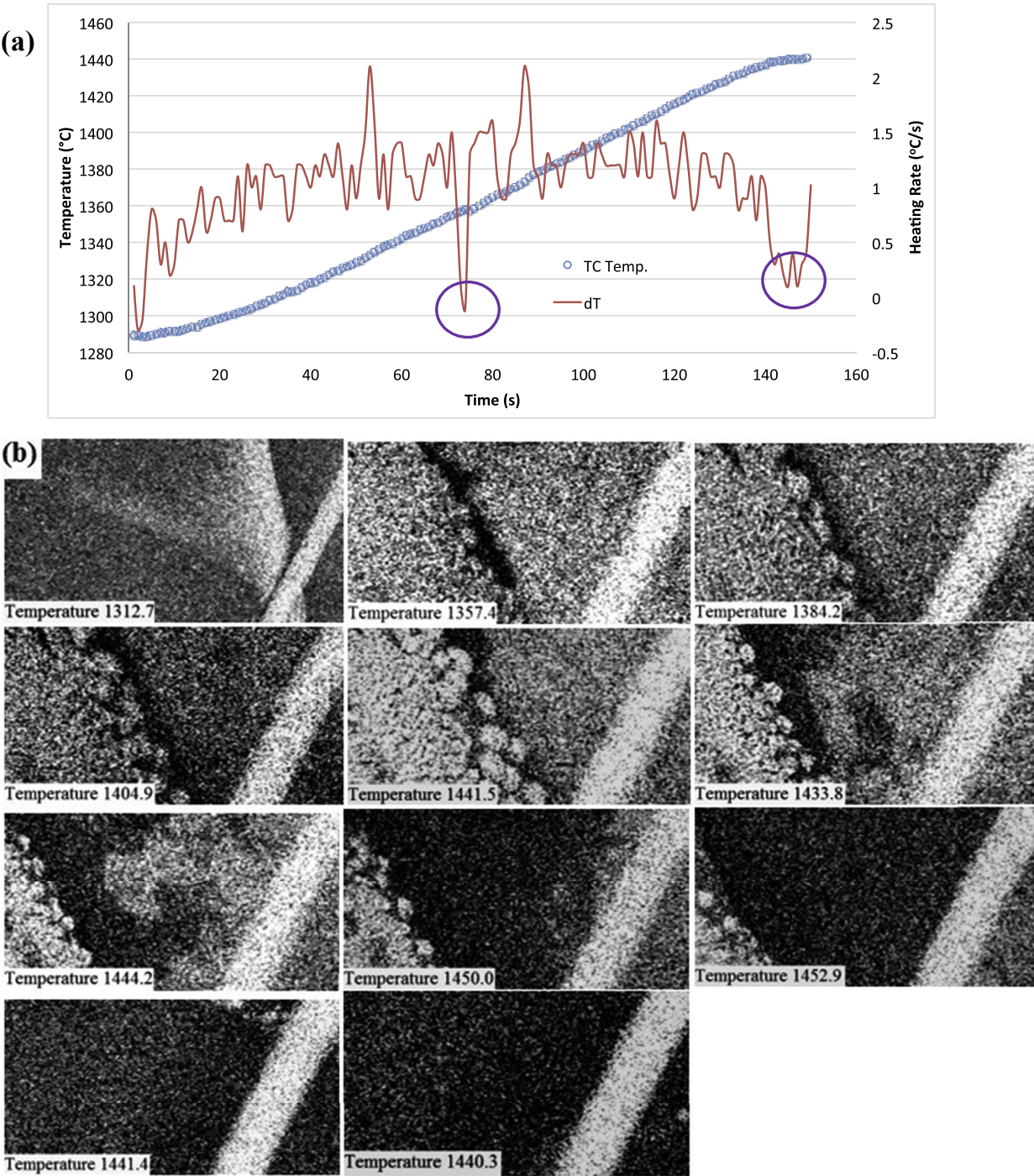
Fig. 1. Behaviour of sample B in a course of first melting; (a) Temperature/Time Differentiation; (b) sequence of frames from SEM images.

composition of different crystals and phases demonstrated in Figs. 2–4. According to Fig. 2 Sample A has three different phases after the melting and solidification and for each phase chemical

Table 3
Melting point of samples in initial and completed melting.

Melting Point	Initial Melting	Completed Melting	Basicity (CaO/SiO$_2$)
Sample A	1389 °C	1415 °C	1.12
Sample B	1357 °C	1440 °C	1.22
Sample R	1326 °C	1411 °C	1.09

composition is listed. Sample A absorbed the MgO and Al$_2$O$_3$ for building the crystal shape, and the dark area of images have higher MgO and Al$_2$O$_3$ evident in the images (a) and (b). The SiO$_2$ was ejected from the top of the crystals. Fig. 3 shows sample B after melting and solidification with different phases and the chemical composition of crystals. The pyramid and dendrite are two types of crystal phases observed in this sample. The pyramid ejected the MgO to build the shape with the top of the pyramid showing no presence of MgO. On the other part of the sample, the dark area has more MgO in comparison with the bright area. In Fig. 4 sample R is shown after melting and solidification with different phases and
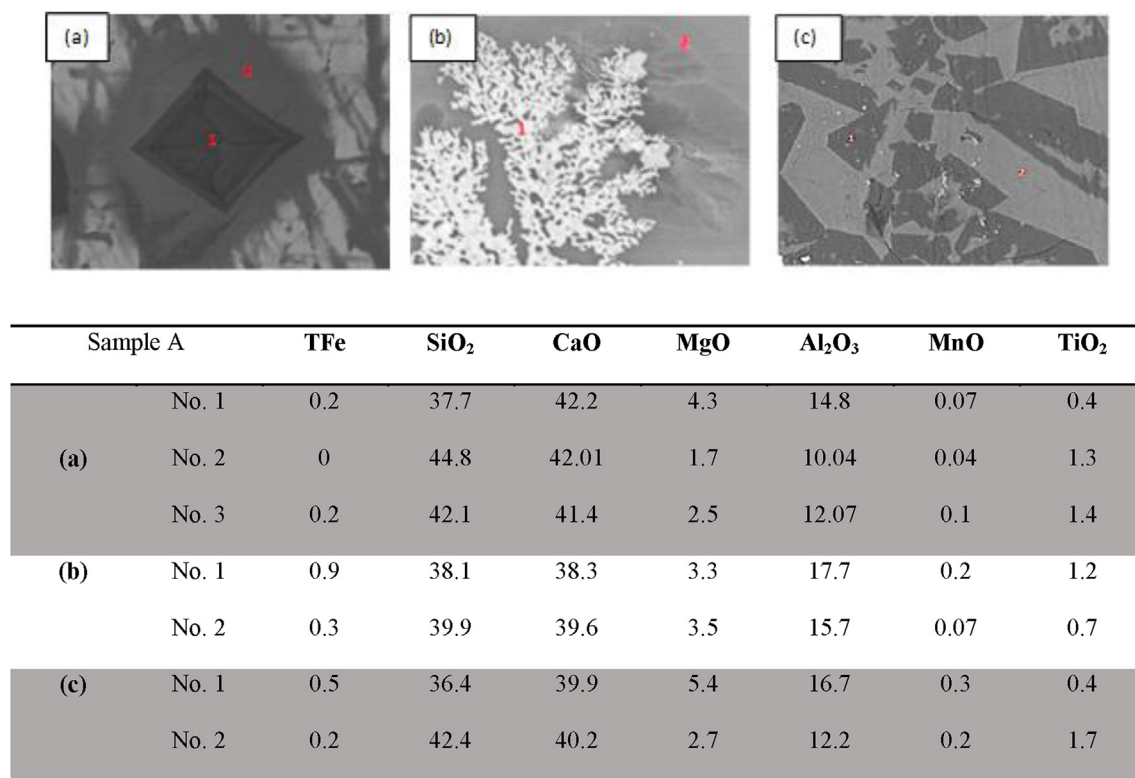
Sample A		TFe	SiO$_2$	CaO	MgO	Al$_2$O$_3$	MnO	TiO$_2$
(a)	No. 1	0.2	37.7	42.2	4.3	14.8	0.07	0.4
	No. 2	0	44.8	42.01	1.7	10.04	0.04	1.3
	No. 3	0.2	42.1	41.4	2.5	12.07	0.1	1.4
(b)	No. 1	0.9	38.1	38.3	3.3	17.7	0.2	1.2
	No. 2	0.3	39.9	39.6	3.5	15.7	0.07	0.7
(c)	No. 1	0.5	36.4	39.9	5.4	16.7	0.3	0.4
	No. 2	0.2	42.4	40.2	2.7	12.2	0.2	1.7

Fig. 2. Sample A phases and chemical composition.

chemical composition. In this sample, the pyramidal crystals also ejected the MgO and Al$_2$O$_3$. The area surrounding the pyramid crystals has a high amount of Al$_2$O$_3$, while the dark area has more MgO and Al$_2$O$_3$ in comparison with the brighter area.

The reason for the decrease in the amount of MgO could be the ejection of this content from the crystalline phase for building their structure. This applies especially for the pyramid crystals in samples B and R, which have the lowest MgO and Al$_2$O$_3$ in comparison to their surroundings. However, the crystalline phase of sample A with crystals and lake around the crystals shows opposing amounts

Sample B		TFe	SiO$_2$	CaO	MgO	Al$_2$O$_3$	MnO	TiO$_2$
(a)	No. 1	0.06	48.2	39.2	1.5	8.9	0.02	1.9
	No. 2	0.04	50.2	39.9	0.4	8.01	0.09	1.2
(b)	No. 1	0.1	49.4	40.3	0.5	8.4	0.06	0.9
	No. 2	0.07	48.08	40.2	1.4	8.7	0	1.4
(c)	No. 1	0.07	31.5	39.9	3.6	24.5	0.09	0.09
	No. 2	0.1	44.1	41.4	0.9	11.9	0.06	1.2

Fig. 3. Sample B phases and chemical composition.

	Sample B	TFe	SiO$_2$	CaO	MgO	Al$_2$O$_3$	MnO	TiO$_2$
(a)	No. 1	0.4	44.9	36.4	0.02	17.2	0.1	0.7
	No. 2	0.02	35.6	35.6	1.2	26.9	0.1	0.3
(b)	No. 1	0.07	47.1	35.2	0.3	15.1	0.05	1.9
	No. 2	0.01	41.5	31.9	2.1	23.7	0.1	0.4
(c)	No. 1	0.04	47.1	35.4	0.1	15.4	0.1	1.6
	No. 2	0.04	37.3	34.5	1.4	26.08	0.07	0.5

Fig. 4. Sample R phases and chemical composition.

of MgO and Al$_2$O$_3$. These types of crystals absorb the MgO and Al$_2$O$_3$ from the surrounding lake and incorporated them in the crystal build up.

3.3. Trace elements analysis

The trace elements of the samples are shown in Table 4. The trace element concentrations can be used to perform the environmental assessment based on the Ecological Investigation Level (EIL) and the Health Investigation Level (HIL), as presented by the Contaminated Sites Management Series (2010). The EIL is the threshold value above which adverse ecological effects are expected, while HIL is the threshold value in waste materials above which human health impacts are expected (Contaminated Sites Management Series, 2010). According to these assessment guidelines, barium, in all three samples, was found to be above the EIL, while manganese in all three samples was above both EIL and HIL. Sample R exceeded the threshold of EIL for the vanadium content.

The environmental concern of Ba is mainly associated to inhibiting the growth of some plant species due to excess amounts of Ba (Pendias, 2011). The possible toxicity of this element could be reduced by adding Mg, Ca, and S salt to the soil. Mn in small concentrations is essential nutrient for plant growth, which may become toxic after exceeding the threshold values. Both Ba and Mn are mobile in acidic soils, while vanadium is absorbed more rapidly under the same conditions (Pendias, 2011).

3.4. Thermal analysis

Fig. 5 shows the specific heat of each sample determined by the Computer Aided Thermal Analysis.

The specific heats show the endothermic and exothermic behaviour of the samples at different temperatures, as presented in Table 5. All samples first exhibited a small endotherm at a temperature range of 727–830 °C followed by a sharp exotherm from 830 to 950 °C. It was only in case of sample B when a third reaction, largely exothermic, occurred in the temperature range between 1108 and 1140 °C.

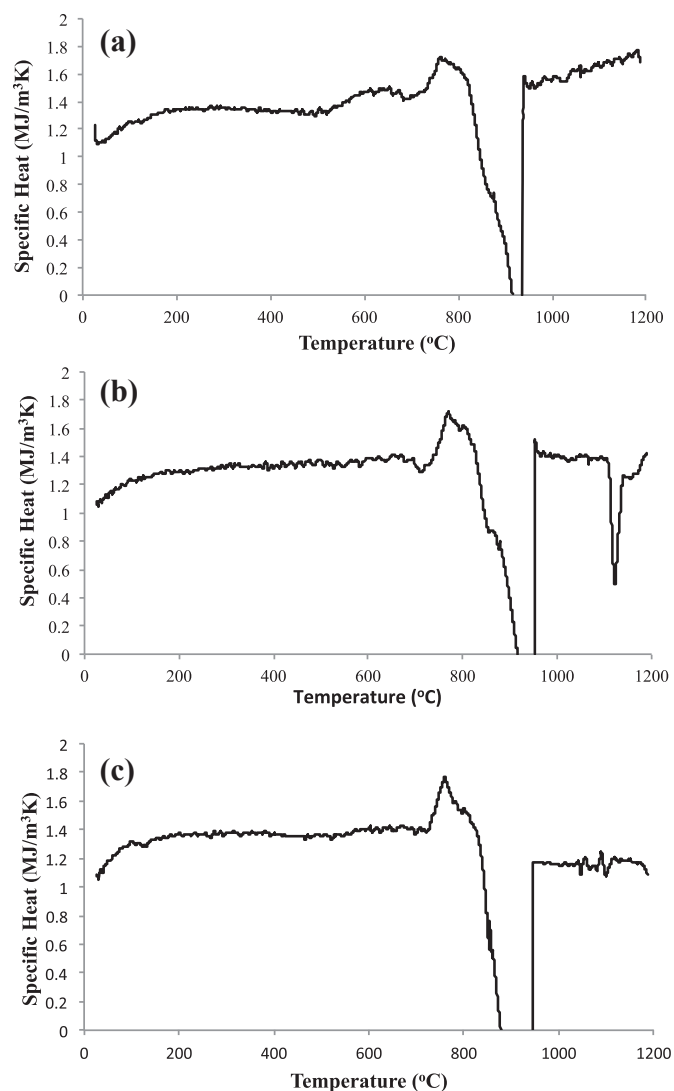### 3.5. Fourier transfer infrared spectroscopy

Fig. 6 shows the FTIR spectra for BFS for a wavenumber range between 1200 and 400 cm^{-1} for the three samples prepared at temperatures which differentiated the thermal regions of activity, as identified with the thermal analysis results. For samples A and R there was no change at 1010 °C in their specific heat, consequently, the FTIR was not performed for these two samples for this temperature. The wavenumber regions have a different type of vibration, as determined by Park et al. (2012), such as symmetric stretching bands of [SiO$_4$]-tetrahedra, asymmetric stretching of [AlO$_4$]-tetrahedra and the symmetric Si-O bending vibration. The wavenumber between 1200 and 800 cm^{-1} relates to the [SiO$_4$]-tetrahedra symmetric stretching vibration bands. The Si-O bending vibration associated with the high degree of polymerisation and depth of FTIR transmittance shows that, from 600 to 520 cm^{-1}, the slag becomes depolymerised. The wavenumber of 400–600 cm^{-1} is related to the Si-O-Si and Si-O-Al connection (Yue et al., 2014). Additionally, 600-800 cm^{-1} is linked to the establishment of Si-O-Al from SiO$_4$ and AlO$_4$ tetrahedral (Yue et al., 2014). According to the previous experiments, the increase of SiO$_2$ causes the growth in the 600-800 cm^{-1} wavenumber region (Yue et al., 2014). The region of 800–1300 cm^{-1} is assigned to the vibration of SiO$_4$ tetrahedra with a varying number of non-bridging oxygens. In summary, the increase in the SiO$_2$ content will increase the network rigidity (Yue et al., 2014). According to Memon et al. (2013) there is internal vibration at 963 cm^{-1} and 494 cm^{-1} due to the [SiO$_4$]$^{4-}$ and [AlO$_5$]$^{5-}$ tetrahedra. 963 cm^{-1} is related to antisymmetric stretching vibration of Si(Al)-O, and the 494 cm^{-1} is related to the vibration of Si-O-Si (Memon et al., 2013). The weak band, at 711 cm^{-1}, is related to the symmetric stretching vibration of Si-O-Si, and 876 cm^{-1} is related to the asymmetric stretch of the AlO$_4$^{1} group (Memon et al., 2013).

Table 4
The trace elements of each sample.

mg/kg	Sample A	Sample B	Sample R	EIL	HIL
Aluminium	79,400	89,100	110,600	–	–
Antimony	<0.5	<0.5	<0.5	–	31
Arsenic	0.93	1.1	1.2	20	400
Barium	440	530	580	300	–
Beryllium	7.6	9.1	7.1	–	80
Bismuth	<0.5	<0.5	<0.5	–	–
Boron	89	88	150	–	12,000
Cadmium	<0.5	<0.5	<0.5	3	80
Calcium	291,800	301,800	245,800	–	–
Cerium	93	110	120	–	–
Cesium	0.53	<0.5	<0.5	–	–
Chromium	9.1	7.9	26	1	400
Cobalt	15	13	14	50	400
Copper	<0.5	0.52	0.51	100	4000
Dysprosium	7.4	9.2	8.3	–	–
Erbium	4.9	6.2	5.3	–	–
Europium	1.9	2.5	2.3	–	–
Gadolinium	8.9	11	10	–	–
Gallium	3.9	4.7	4.7	–	–
Germanium	1.7	2.2	2	–	–
Gold	<0.5	<0.5	<0.5	–	–
Hafnium	0.52	0.63	0.62	–	–
Holmium	1.6	2	1.8	–	–
Iridium	<0.5	<0.5	<0.5	–	–
Iron	2510	3210	2840	–	–
Lanthanum	45	56	49	–	–
Lead	<0.5	<0.5	<0.5	600	1200
Lithium	71	60	73	–	–
Lutetium	0.77	0.97	0.84	–	–
Magnesium	54,400	55,700	86,800	–	–
Manganese	1980	2030	7610	–	–
Mercury	0.35	0.31	0.4	1	60
Molybdenum	<0.5	<0.5	<0.5	40	–
Neodymium	36	45	41	–	–
Nickel	<0.5	<0.5	<0.5	60	2400
Niobium	<0.5	<0.5	<0.5	–	–
Palladium	<0.5	<0.5	<0.5	–	–
Phosphorus	40	92	140	2000	–
Platinum	<0.5	<0.5	<0.5	–	–
Potassium	4150	4080	4620	–	–
Rhodium	<0.5	<0.5	<0.5	–	–
Rubidium	14	12	14	–	–
Ruthenium	<0.5	<0.5	<0.5	–	–
Samarium	7.1	9	8.3	–	–
Scandium	16	20	31	–	–
Selenium	4.6	5.5	3.6	–	–
Silicon	2900	2850	2870	–	–
Silver	<0.5	<0.5	<0.5	–	–
Sodium	3850	3810	4890	–	–
Strontium	820	880	510	–	–
Sulphur	11,900	15,900	10,500	600	–
Tantalum	<0.5	<0.5	<0.5	–	–
Tellurium	<0.5	<0.5	<0.5	–	–
Terbium	1.3	1.5	1.4	–	–
Thallium	<0.5	<0.5	<0.5	–	–
Thorium	15	17	23	–	–
Thulium	0.73	0.9	0.8	–	–
Tin	<0.5	<0.5	<0.5	50	–
Titanium	2690	2960	5340	–	–
Tungsten	79	85	92	–	–
Uranium	14	13	9.5	–	–
Vanadium	13	20	79	50	–
Ytterbium	4.7	5.9	5.4	–	–
Yttrium	49	61	51	–	–
Zinc	3	8.7	2.1	200	28,000
Zirconium	24	31	29	–	–

Fig. 5. Specific heat of blast furnace slags, (a) sample A, (b) sample B and (c) sample R.

450 cm^{-1} is to Si-O-Si and Si-O-Al connections. The changes in transmittance at wavenumbers of 916, 687, and 450 cm^{-1} is larger in sample A than samples B and R, likely because sample A had the highest amount of SiO_2 and the lowest amount of Al_2O_3, comparing to the other two samples. On the other hand, sample R with the lowest amount of SiO_2 and highest amount of Al_2O_3 had the lowest change in transmittance in the mentioned wavenumbers. Consequently, the increase in the content of SiO_2 increased network rigidity in all three samples. The significant variations of transmittance in the three mentioned wavenumbers for all three samples coincided with the exothermic behaviour of the samples.

Table 5
Temperature range of thermal activity and heats of reactions of each sample.

	Temperature Range (°C)	ΔH (MJ/m^3)
Sample A	727−828	18.1
	829−938	−515
Sample B	735−829	17.5
	821−954	−447
	1108−1140	−12
Sample R	729−808	10.2
	836−949	−140

The FTIR spectroscopy for the three samples showed the major changes in the spectra with wavenumbers at 916, 687, and 450 cm^{-1}. According to Yue et al. (2014) the 916 cm^{-1} wavenumber is related to the [SiO$_4$]-tetrahedra and 687 cm^{-1} to the establishment of Si-O-Al from [SiO$_4$]-tetrahedra. The wavenumber at
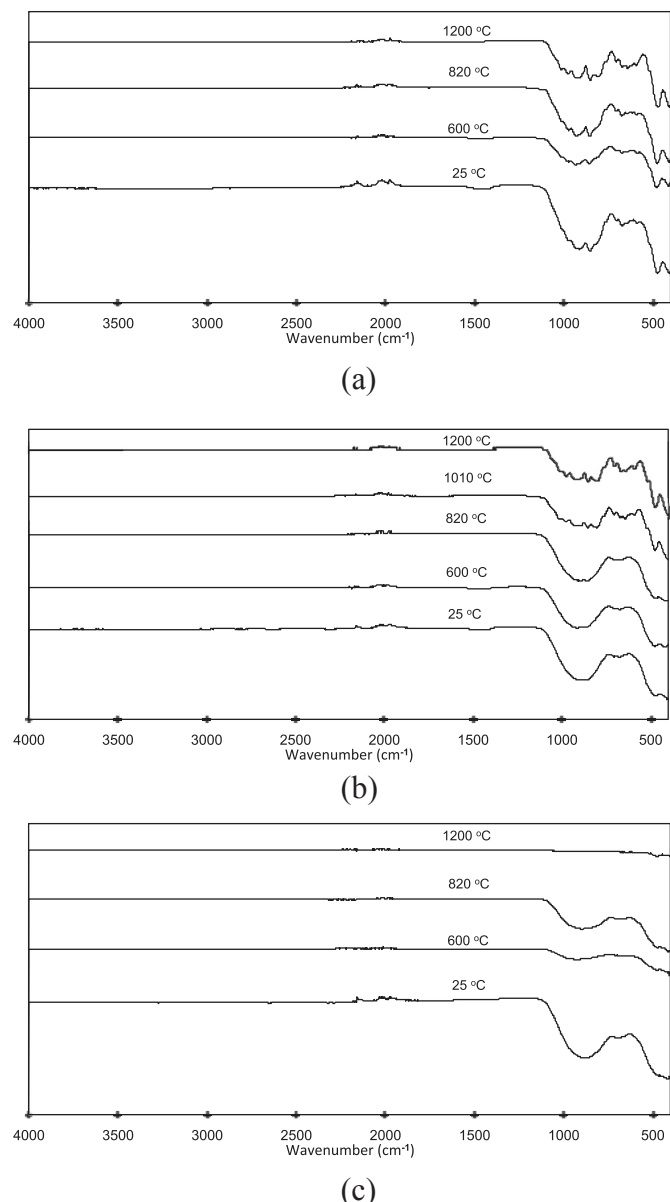
(a)

(b)

(c)

Fig. 6. FTIR spectroscopy of blast furnace samples (a) sample A, (b) sample B and (c) sample R.

4. Conclusions and recommendations

This study investigated the thermal properties and *in-situ* morphology phase transformations at the melting-crystallisation processes during cooling of the industrial grade blast furnace slag, as an initial investigation towards optimisation of the heat energy recovery during the process of heating the liquid pig iron. This study revealed that the basicity of the blast furnace slag has direct effect on the melting interval of the slag as higher basicity increases the initial melting temperature. The high amount of Al_2O_3 and MgO have an effect on and increased the melting interval of the BFS. The amount of MgO in the crystalline part of the cooled slag is remarkably low in comparison to the initial amounts before the heating and cooling processes. This is because the slag rejects the MgO for building the crystalline phase during the solidification process. During heating, the BFS samples exhibited small endothermic reaction at a temperature

range of 727—830 °C followed by a significant exothermic behaviour at a temperature range of 830 °C and 950 °C. Sample B additionally exhibited an additional significant exothermic reaction at a temperature range of 1108 and 1140 °C. When the thermal analysis data was compared to the FTIR analysis, it is evident that the amount of SiO_2 had an effect on the exothermic behaviour, especially for the 916 cm^{-1} wavenumber. According to the specific heat and thermal analysis, all three samples have the exothermic energy between 140 and 515 MJ/m^3 that provide additional opportunity for reuse. The waste energy in the BFS can be reused for reducing the energy input for heating the pig iron or in other applications in the iron and steel plant, such as pre-heating the air.

References

Baati, M., Esfahani, S., Utigard, T., 2011. Energy recovery from high temperature slags. Energy 36, 5440—5449.

Coates, J., 2000. Interpretation of Infrared Spectra, a Practical Approach. Encyclopedia of Analytical Chemistry. John Wiley & Sons Ltd, Chichester, UK 10815-10837.

Contaminated Sites Management Series, 2010. Assessment Levels for Soil, Sediment and Water. www.esdat.net/Environmental%20Standards/Australia/WA/Assessment%20Levels%20-%202010.pdf (Date accessed 15 August 2016).

Crossin, E., 2015. The greenhouse gas implications of using ground granulated blast furnace slag as a cement substitute. J. Clean. Prod. 95, 101—108.

Dai, B., Zhang, J., 2012. The research of blast furnace slag fluidity by viscosity experiment and phase diagram analysis. Metall. Int. XVII, 25—28.

Dimitrova, S., 1995. Metal sorption on blast-furnace slag. Water Res. 30, 228—232.

Dippenaar, R., 2005. Industrial uses of slag (the use and re-use of iron and steel-making slags). Ironmak. Steelmak. 32, 35—46.

Francis, A., 2005. Non-isothermal crystallization kinetics of a blast furnace slag glass. J. Am. Ceram. Soc. 88, 1859—1863.

Iron Ore, Global Market, 2015. Iron Ore Facts. www.ironorefacts.com/the-facts/iron-ore-global-markets (Date accessed 16 December 2015).

Ito, T., Yotsuji, J., Nagamune, A., 2014. Development of pig iron and molten slag level measurement technique for blast furnace. ISIJ Int. 54, 2618—2622.

Jak, E., Hayes, P., 2004. Phase equilibria determination in complex slag systems. In: paper presented at International Conference on Molten Slags Fluxes and Salts, 117. South African Institute of Mining and Metallurgy, pp. 1—17.

Kan, T., Strezov, V., Evans, T., Nelson, P., 2015. Trace element deportment and particle formation behaviour during thermal processing of iron ore: technical reference for risk assessment of iron ore processing. J. Clean. Prod. 102, 384—393.

Kim, J., Lee, Y., Min, D., Jung, S., Yi, S., 2004. Influence of MgO and Al_2O_3 contents on viscosity of blast furnace type slags containing FeO. ISIJ Int. 44, 1291—1297.

Kriskova, L., Pontikes, Y., Pandelaers, L., Cizer, O., Jones, P., Balen, K., Blanpain, B., 2013. Effect of high cooling rates on the mineralogy and hydraulic properties of stainless steel slags. Metall. Mater. Trans. B 44B, 1173—1184.

Kuo, Y., Wang, J., Wang, C., Tsai, C., 2007. Effect of water quenching and SiO_2 addition during vitrification of fly ash Part 1: on the crystalline characteristics of slags. J. Hazard. Mater. 152, 994—1001.

Liapis, I., Papayianni, I., 2015. Advances in chemical and physical properties of electric arc furnace carbon steel slag by hot stage processing and mineral mixing. J. Hazard. Mater. 283, 89—97.

Madejova, J., 2003. FTIR techniques in clay mineral studies. Vib. Spectrosc. 31, 1—10.

Memon, S., Loa, T., Barbhuiya, S., Xu, W., 2013. Development of form-stable composite phase change material byincorporation of dodecyl alcohol into ground granulated blast furnace. Energy Build. 62, 360—367.

Motz, H., Geiseler, J., 2001. Products of steel slags an opportunity to save natural resources. Waste Manag. 21, 285—293.

Ozturk, Z., Gultekin, E., 2015. Preparation of ceramic wall tiling derived from blast furnace slag. Ceram. Int. 41, 12020—12026.

Park, H., Park, J., Kim, G., Shon, I., 2012. Effect of TiO2 on the viscosity and slag structure in blast furnace type slags. Steel Res. Int. 83, 150—156.

Pendias, A., 2011. Trace Elements in Soils and Plants, fourth ed. CRC Press, United States of America.

Sadek, D., 2014. Effect of cooling technique of blast furnace slag on the thermal behavior of solid cement bricks. J. Clean. Prod. 79, 134—141.

Strezov, V., 2006. Iron ore reduction using sawdust: experimental analysis and kinetic modelling. Renew. Energy 31, 1892—1905.

Wagner, L., 1999. Failure Analysis of Integrated Circuits, on Ngo, P. Energy Dispersive

Spectroscopy. publishing Springer, New York, United States of America, pp. 205—206.

Yue, Y., Zhang, X., Xu, Y., Huang, S., Chen, P., 2014. Structural, dielectric and melting properties of aluminosilicate glasses based on blast furnace slag for printed circuit board applications. Mater. Lett. 136, 356—358.

Zhao, H., Sun, W., Wu, X., Gao, B., 2015. The properties of the self-compacting concrete with fly ash and ground granulated blast furnace slag mineral admixtures. J. Clean. Prod. 95, 66—74.